INTERNATIONAL JOURNAL FOR NUMERICAL METHODS IN FLUIDS, VOL. 14, 47–69 (1992)

A ONE-DIMENSIONAL MOVING GRID SOLUTION FOR THE COUPLED NON-LINEAR EQUATIONS GOVERNING MULTIPHASE FLOW IN POROUS MEDIA. 2: EXAMPLE SIMULATIONS AND SENSITIVITY ANALYSIS

AMIR GAMLIEL

Electronic Data Systems Corporation, Environmental Science Department, GM Research Laboratories, Warren, MI 48090-9055, U.S.A.

AND

LINDA M. ABRIOLA

Department of Civil Engineering, The University of Michigan, Ann Arbor, MI 48109, U.S.A.

SUMMARY

This paper presents numerical examples for the moving grid finite element algorithm derived in Part 1 to solve the non-linear coupled set of PDEs governing immiscible multiphase flow in porous media in one dimension. Examples include single- and double-front simulations for two- and three-phase flow regimes and incorporating a mass sink. The modelling approach is shown to achieve significant savings in computation time and memory allocation when compared with fixed grid solutions of equivalent accuracy. This work includes sensitivity analyses for the parameters which are incorporated in the grid adaptation method, including the curvature weights, artificial viscosity and artificial repulsive force. It is found that the curvature weights are exponential functions of the negative ratio of the square root of the domain length to the number of discrete nodes. These weighting parameters are also shown to depend upon the shape of the front. On the basis of the examined simulations, it is recommended that artificial viscosity be neglected in the solution of the coupled non-linear set of PDEs governing multiphase flow in porous media. Similarly, use of a repulsive force is found to be unnecessary in simulations involving the migration of two liquid phases. For multiphase flows incorporating a gas phase it is recommended to use a non-zero value for the repulsive force to avoid development of an ill-conditioned nodal distribution matrix. An equation to evaluate the repulsive force under these circumstances is suggested.

KEYWORDS Partial differential equations Non-linear equations Coupled system Numerical methods Finite elements Adaptive grid Flow in porous media Groundwater contamination Multiphase flow Immiscible flow

1. INTRODUCTION

The use of adaptive grid methods for the solution of multiphase flow equations in porous media has not been fully explored in the literature. This is primarily due to the non-linear and coupled nature of such problems. It is apparent, however, that distinct advantages are to be gained by the application of such techniques to the resolution of sharp fronts present in many of these problems. In Part 1 of this paper a moving grid finite element method (MGFEM) was developed and applied to the coupled set of partial differential equations governing immiscible flow and incorporating capillarity. The governing equations along with auxiliary relations (repeated here

0271–2091/92/010047–23$11.50
© 1992 by John Wiley & Sons, Ltd.
Received 13 September 1989
Revised 12 February 1991

for convenience) are

$$\phi\left(\frac{\partial S_w}{\partial P_{ow}}\frac{\partial P_{ow}}{\partial t}+\frac{\partial S_w}{\partial P_{wg}}\frac{\partial P_{wg}}{\partial t}+S_w\beta_{s_w}\frac{\partial P_{wg}}{\partial t}\right)=\frac{\partial}{\partial x}\left[K_w\left(\frac{\partial P_{wg}}{\partial x}+\gamma_w\cos\theta\right)\right], \tag{1a}$$

$$\phi\left(\frac{\partial S_o}{\partial P_{ow}}\frac{\partial P_{ow}}{\partial t}+\frac{\partial S_o}{\partial P_{wg}}\frac{\partial P_{wg}}{\partial t}+S_o\beta_{s_o}\frac{\partial (P_{ow}+P_{wg})}{\partial t}\right)=\frac{\partial}{\partial x}\left[K_o\left(\frac{\partial (P_{ow}+P_{wg})}{\partial x}+\gamma_o\cos\theta\right)\right], \tag{1b}$$

$$S_\alpha=Sr_\alpha+\frac{Ss_\alpha-Sr_\alpha}{[1+(a_{s_\alpha}h_c)^{n_{S_\alpha}}]^{m_{S_\alpha}}}, \tag{1c}$$

$$\sum_{\alpha=1}^{N_\alpha} S_\alpha=1, \tag{1d}$$

$$kr_\alpha=\frac{\{1-(a_{k_\alpha}h_c)^{n_{k_\alpha}-1}[1+(a_{k_\alpha}h_c)^{n_{k_\alpha}}]^{-m_{k_\alpha}}\}^2}{[1+(a_{k_\alpha}h_c)^{n_{k_\alpha}}]^{m_{k_\alpha}/2}}, \tag{1e}$$

where $\beta_{s_w}=\beta_w+\beta_\phi$ and $\beta_{s_o}=\beta_o+\beta_\phi$. The notation is summarized at the end of Part 1 of this paper. In the developed model the above equations are solved using a standard linear Galerkin finite element discretization in space and a backward difference operator in time.

The moving grid algorithm is based upon the combination of two equidistribution criteria, one in the variable gradient and one in the curvature. To facilitate application of this algorithm, a representative gradient (P') is selected, based on the largest gradient among the primary variables at a given location. The following set of algebraic equations for the nodal positions are formed from these criteria:

$$x_1=x(0), \tag{2a}$$

$$f_{i-1}-f_i=0 \quad \text{for } i=2,\ldots,n-1, \tag{2b}$$

$$x_n=x(n), \tag{2c}$$

where the explicit form of (2b) is

$$\begin{aligned}
&x_{i-2}\{-B_1\sqrt{[(P'_{i-1}-P'_{i-2})^2+\varepsilon_2]}\}\\
&+x_{i-1}\{-\sqrt{(P'^2_{i-1}+\varepsilon_1)}+(B_1-B_2)\sqrt{[(P'_i-P'_{i-1})^2+\varepsilon_2]}\}\\
&+x_i\{\sqrt{(P'^2_{i-1}+\varepsilon_1)}+\sqrt{(P'^2_i+\varepsilon_1)}+B_1\sqrt{[(P'_{i-1}-P'_{i-2})^2+\varepsilon_2]}+B_2\sqrt{[(P'_{i+1}-P'_i)^2+\varepsilon_2]}\}\\
&+x_{i+1}\{-\sqrt{(P'^2_i+\varepsilon_1)}+(B_2-B_1)\sqrt{[(P'_i-P'_{i-1})^2+\varepsilon_2]}\}\\
&+x_{i+2}\{-B_2\sqrt{[(P'_{i+1}-P'_i)^2+\varepsilon_2]}\}=0.
\end{aligned} \tag{2d}$$

Here $P'=(P_{i+1}-P_i)/(x_{i+1}-x_i)$. Because nodal estimates of pressures are required for the solution of (2), these equations must be solved in some iterative manner with the governing equations (1).

A two-phase, single-front displacement was simulated as an example application of the moving grid approach in Part 1 and is referred to herein as simulation case 1. For this example the model performed quite well, achieving a substantial saving in computer time and storage for a desired degree of accuracy. Clearly, however, a much greater range of simulations must be examined to demonstrate the utility of the modelling approach. In the following pages a number of model simulations are presented for various scenarios which are representative of two- and three-phase flow problems incorporating multiple fronts and sources/sinks. There is a distinct absence of literature on the application of moving grid methods to these more complex types of flow scenarios.

Another important issue examined herein is the estimation of moving grid algorithm parameters. These parameters include artificial viscosity and repulsive force coefficients ($\varepsilon_1, \varepsilon_2$) and curvature weights (B_1, B_2). Relatively little attention has been directed towards the development of guidelines for the selection of these parameters. Constant values for each parameter are often used (see e.g. References 1–4) and these values are frequently determined by a trial-and-error procedure. In this work the solution sensitivity to these parameters is explored through numerical experimentation, and some tentative parameter selection guidelines are suggested for the solution of immiscible phase flow problems.

Sensitivity analysis

In order to examine the influence of moving grid parameters on solution efficiency and accuracy, it will be useful to revisit the example simulation presented in case 1. Simulation matrix and fluid properties and boundary conditions are given in Tables I and II. Subsequent simulations, unless otherwise noted, are also based upon these same parameters. Functional forms of saturation and relative permeability functions are given in equations (1c)–(1e). A solution for one set of moving grid parameters is plotted in Figure 1. The values of the parameters used to obtain this solution are $\varepsilon_1 = 0$, $\varepsilon_2 = 0$, $B_1 = 1{\cdot}2 \times 10^{-4}$ and $B_2 = 10^{-4}$. These moving grid parameters were determined through numerical experimentation and comparison with a fine fixed grid finite element method (FGFEM) simulation of high accuracy.

From these numerical experiments some general observations may be made relating to parameter selection.

1. The nodes tend to concentrate at the sharp gradient (front) area as ε_1 becomes smaller. As the nodal spacing decreases at the front, numerical dispersion also decreases and the front becomes steeper. This response to ε_1 has also been observed by others (e.g. Reference 5).
2. As B_1 and B_2 become larger, the nodes tend to concentrate to a greater degree at large-curvature areas and to a lesser degree at steep gradient areas. This behaviour can be deduced directly from equations (2) since B_1 and B_2 are the weight parameters for the curvature criterion in the equidistribution function. To illustrate this behaviour, simulation results for different values of $B_1 = B_2 = B$ are shown in Figure 2.
3. The nodal spacing at the front becomes larger as the artificial viscosity (ε_2) increases.
4. The smallest nodal spacing also depends upon two additional factors: the ratio between the domain length and the number of discrete nodes (L/n) and the second derivative of the function on which the equidistribution function is based, i.e. the ratio amongst the values of P_i' in (2). The minimum element length contained within the front decreases with an increase in the number of discrete nodes/domain length or with an increase in the magnitude of the gradient about the front in comparison to the gradients elsewhere in the domain.
5. For this problem the smallest element length increases with time since the propagation front smears with its advancement and the maximum gradient value decreases.

The values of the moving grid parameters could be determined *a priori* by substituting desired nodal locations into (2) and solving for ε_1, ε_2, B_1 and B_2 in order to obtain a specific nodal distribution at the front. In general, this is a rather difficult task since the equidistribution function is non-linear. Such a scheme is also impractical for situations in which the front changes in shape or additional fronts or sources/sinks are introduced into the domain. On the basis of the observations enumerated above, it is alternatively proposed in this work that the values of ε_1 and ε_2 be computed within the programme as quadratic functions of the largest gradient in the domain and that B_1 and B_2 be treated as constants.

Table I. Soil and fluid parameters used in simulations (after Abriola[12])

Characteristic	Value	Units
g	980·616	$cm\,s^{-2}$
ϕ	0·36	
K	$5·2831 \times 10^{-7}$	cm^2
β_ϕ	$2·0 \times 10^{-10}$	$cm^2\,dyn^{-1}$
γ_o	1437·28871	$g\,cm^{-2}\,s^{-2}$
μ_o	$5·8 \times 10^{-3}$	Poise
β_o	0	
γ_w	980·465	$g\,cm^{-2}\,s^{-2}$
μ_w	0·01	Poise
β_w	$4·531 \times 10^{-11}$	$cm^2\,dyne^{-1}$
Water–TCE simulation		
Sr_w	0·306	
Ss_w	0·9998	
a_{s_w}	0·11	cm^{-1}
n_{s_w}	6·50	
a_{k_w}	0·108	cm^{-1}
n_{k_w}	6·60	
a_{k_o}	0·40	
Water–TCE gas simulation		
Sr_w	0·170	
Ss_w	1·000	
Sr_o	0·170	
Ss_o	1·000	
a_{s_w}	0·1043	cm^{-1}
n_{s_w}	4·690	
$a_{s_{\text{total liquids}}}$	0·0624	cm^{-1}
$n_{s_{\text{total liquids}}}$	8·6050	
a_{k_w}	0·108	cm^{-1}
$n_{k_w}^{\text{w–o system}}$	0·8560	
$n_{k_w}^{\text{w–g system}}$	0·8838	
$n_{k_o}^{\text{w–o system}}$	0·6320	
$n_{k_o}^{\text{o–g system}}$	0·6216	

The following recommendations are made for the evaluation of the moving grid parameters for the solution of the PDEs that govern two- and three-phase flow in porous media. For the artificial viscosity ε_2 a value of zero is suggested. Use of the artificial viscosity parameter proved to be unnecessary in these simulations since the organic–water front moves relatively slowly and a solution of equations (2) is guaranteed with no nodal overlapping if the matrix problem is not ill-conditioned.

For the artificial repulsive force ε_1 no specific recommendation could be made based on the two-phase flow problem. Representative gradients varied by only three orders of magnitude over the domain for the problem presented in Figure 1. In this problem the initial minimum value of the gradient is about $10\,dyn\,cm^{-3}$ and the minimum gradient increases as the simulation

Table II. Initial and boundary conditions for the problems discussed in this paper

	P_{wg} (dyn cm^{-2})	P_{ow} (dyn cm^{-2})
Case 1		
Initial conditions	1000	0
Upstream boundary conditions	5900	9710
Downstream boundary conditions	10000	0
Case 2		
Initial conditions	Zero at the top and hydrostatic water pressure distribution	0
Upstream boundary conditions	5100	9510
Downstream boundary conditions	44127.7	0
Case 3		
Initial conditions	Results of case 2	Results of case 2
Upstream boundary conditions	15000	7729
Downstream boundary conditions	44127·7	0
Case 4		
Initial conditions	Results of case 1	Results of case 1
Upstream boundary conditions	5900	9710
Downstream boundary conditions	1000	0
Case 5		
Initial conditions	−21135	15210
Upstream boundary conditions	−16830	15210
Downstream boundary conditions	−21135	15210
Case 6		
Initial conditions	Results of case 5	Results of case 5
Upstream boundary conditions	−7500	7500
Downstream boundary conditions	−21135	15210

proceeds. This minimum value and the ratio between the maximum and minimum values of the gradients guarantee that the set (2) is not ill-conditioned. Thus no artificial repulsive force was required in the simulation of this problem. A zero value of ε_1 was not found to be adequate for other problems, however. For example, variations in the representative gradients over five orders of magnitude were found for the simulation of wagter–organic–gas flow (cases 5 and 6), with a minimum gradient of about zero. Zero values for gradients and curvatures produced an ill-conditioned matrix problem for nodal distribution. For this case an optimal ε_1 was found to vary with the square of the maximum gradient in the domain. This variation of ε_1 is consistent with the expression (2d), where summation of ε_1 and the square of the gradient appear within a square root operator. The ratio of the gas and water viscosities was used to scale the gradient in the expression for ε_1. Recall that the gas pressure gradient (gas convection) is neglected in the governing equations. Thus the selection of such a scaling factor is physically based since it represents the gas gradient in subdomains where the water and TCE gradients are near zero. The following

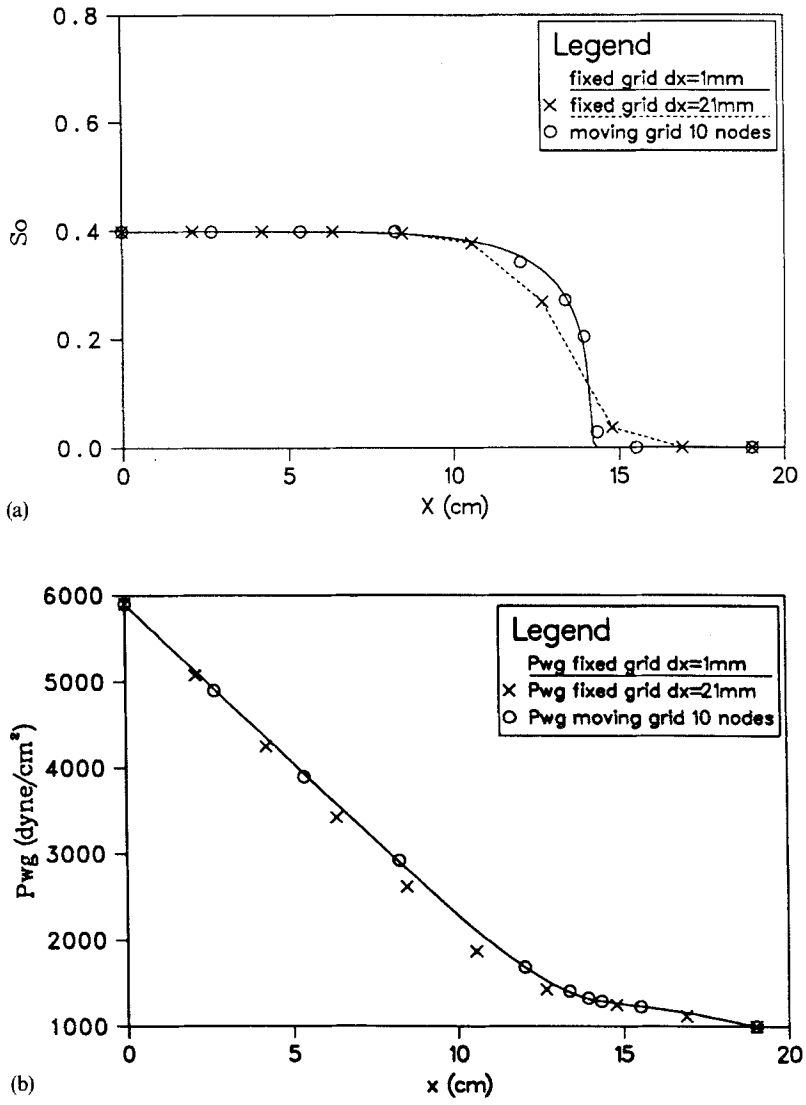

Figure 1. Simulation results for case 1 after 1000 s: (a) S_o; (b) P_{wg}

expression for ε_1, then, was found to give satisfactory results in the three-phase simulations examined:

$$\varepsilon_1 = \left(\frac{\mu_g}{\mu_w} \max \{ P'_{wg} \} \right)^2. \tag{3}$$

Other expressions for ε_1 have been suggested.[5-7] These expressions are first-order functions of the ratio between gradients or element lengths.

For the evaluation of B_1 and B_2, numerical experiments revealed that the curvature weight must be increased with the number of nodes and decreased with the square root of the domain

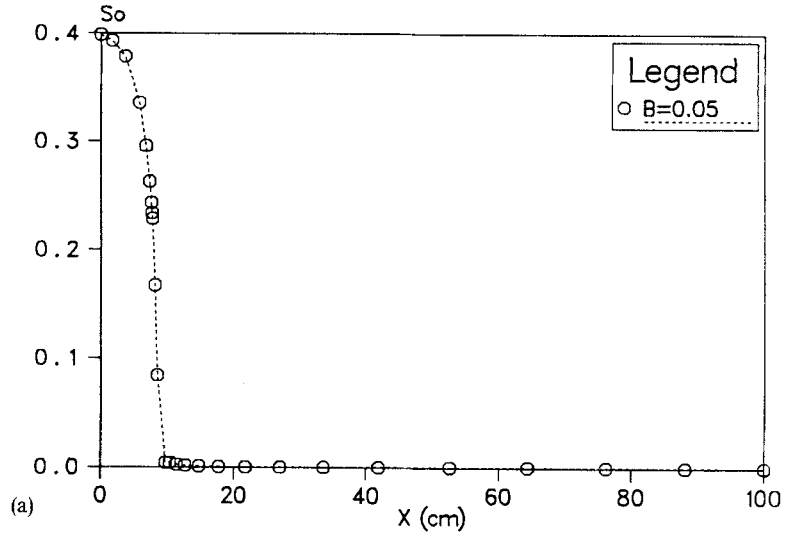

(a)

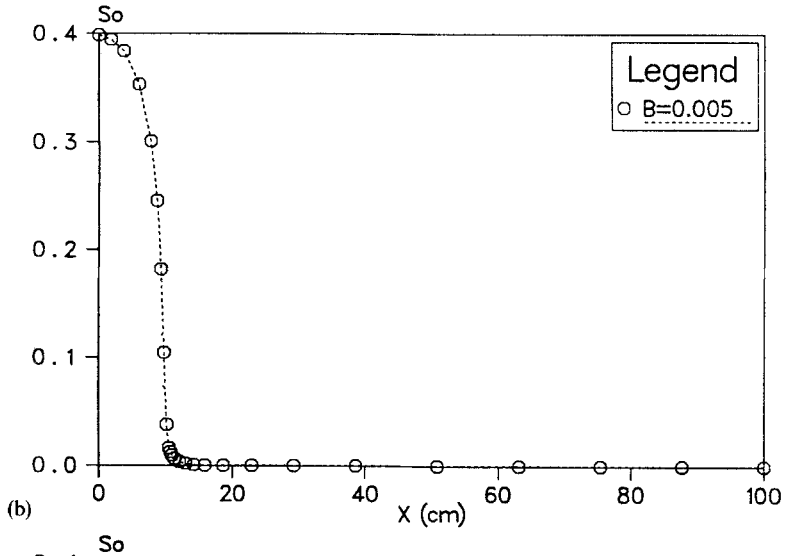

(b)

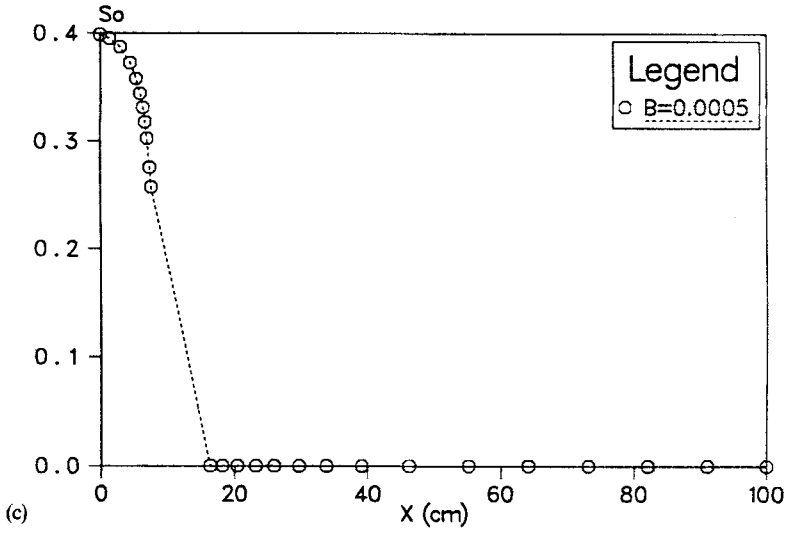

(c)

Figure 2. Effect of curvature weighting: (a) $B = 0{\cdot}05$; (b) $B = 0{\cdot}005$; (c) $B = 0{\cdot}0005$

length in order to achieve more accurate solutions. A summary of the findings pertaining to B_1 and B_2 is given in Figure 3. Here $B_1 = B_2 = B$ and each point represents the results of a number of simulations for which B was varied, keeping all other parameters fixed. The optimal value of B for each group of simulations was selected as that value which produced the smallest error when compared to the fine FGFEM solution. The errors were estimated by integrating the deviations of the MGFEM solution from the fine FGFEM solution.[8]

Numerical experiments were conducted for a variety of parameters that could influence the curvature upstream and downstream of the saturation front between two immiscible fluids. The

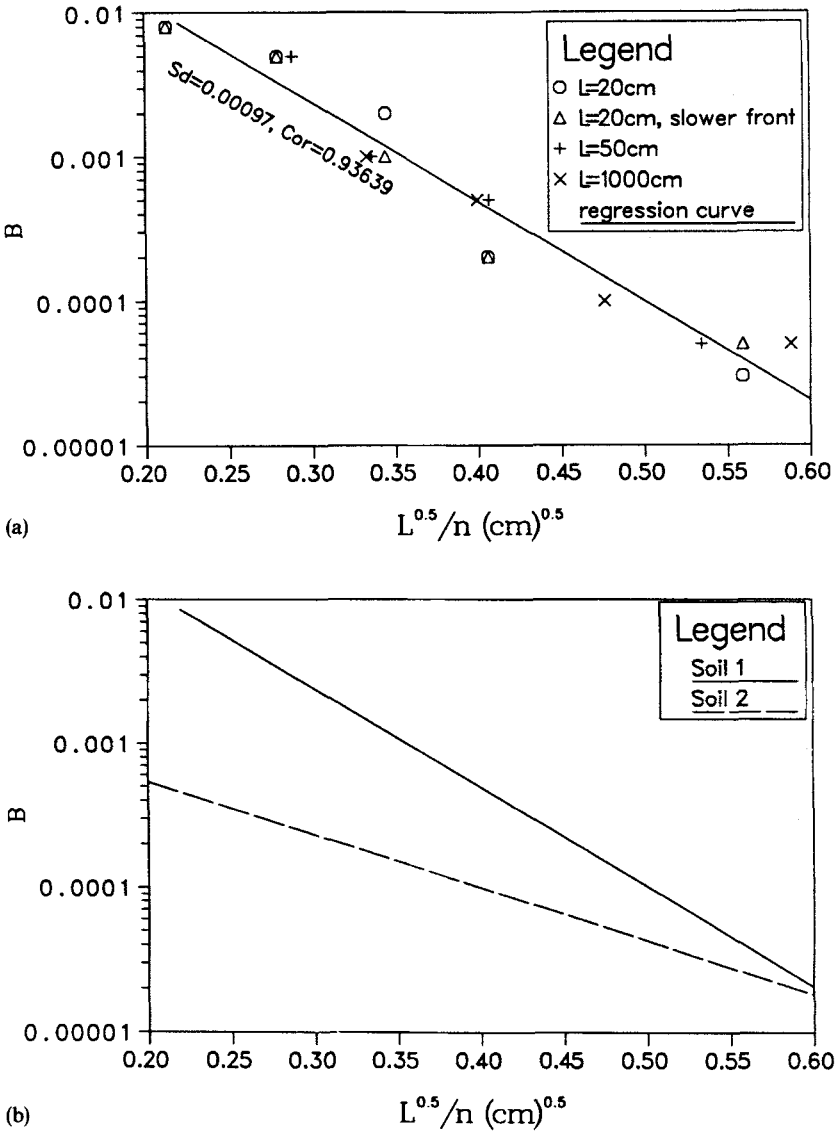

Figure 3. Optimal curvature weight as a function of domain length and number of nodes: (a) for the first soil and water characteristics of Table I; (b) the regression curves for both soils

parameters that were varied in the experiments included the speed of fluid front propagation, the number of nodes, the domain length and the fluid retention curve shape (saturation as a function of capillary pressure). Variations of the front propagation speed and the domain length were included because dimensional analysis of equation (1) shows that the characteristic change of S_α with time depends upon the Reynolds number (see Appendix). Note that variations of viscosity were considered implicitly by varying the retention curves. The two speeds of front propagation considered here are those of the simulation shown in Figure 1 and a 40% slower propagation rate. The front propagation rate was altered by changing the initial and boundary conditions. Domain lengths of 20, 50 and 100 cm were used with different numbers of nodes. The experiments were conducted by varying B over five orders of magnitude in increments from one to one-half an order of magnitude. The values of B which gave the minimum error in the solution are given in Figure 3(a). This figure shows that the optimal values of B do not change with the velocity of the front.

Next, retention curves were varied in the experiments because these curves have a significant influence on the front shape. The front tends to be less sharp and the curvature associated with this front becomes smaller as the retention curve slope becomes more moderate. Retention curves for two soils and the fluid characteristics from Table I were used in these experiments. These retention curves are shown in Figure 4. The characteristics of the first soil were taken from Table I. The second soil is a more graded one (Figure 4). Its characteristic parameters are $\phi = 0{\cdot}3$, $K = 3 \times 10^{-7}\,\mathrm{cm}^2$, $Sr_w = 0{\cdot}3$, $Ss_w = 0{\cdot}9998$, $a_{s_w} = 0{\cdot}05$, $n_{s_w} = 5{\cdot}0$, $a_{k_w} = 0{\cdot}05$, $n_{k_w} = 8{\cdot}0$, $a_{k_o} = 1{\cdot}0$ and $n_{k_o} = 15{\cdot}0$.

Figure 3(b) shows the optimal B regression lines for each soil. One can observe that the curvature weights become smaller with an increase in soil grading (which smears the front) and that the weights depend upon the square root of the domain length divided by the number of nodes and the magnitude of the curvature. Figures 3(a) and 3(b) suggest an exponential function

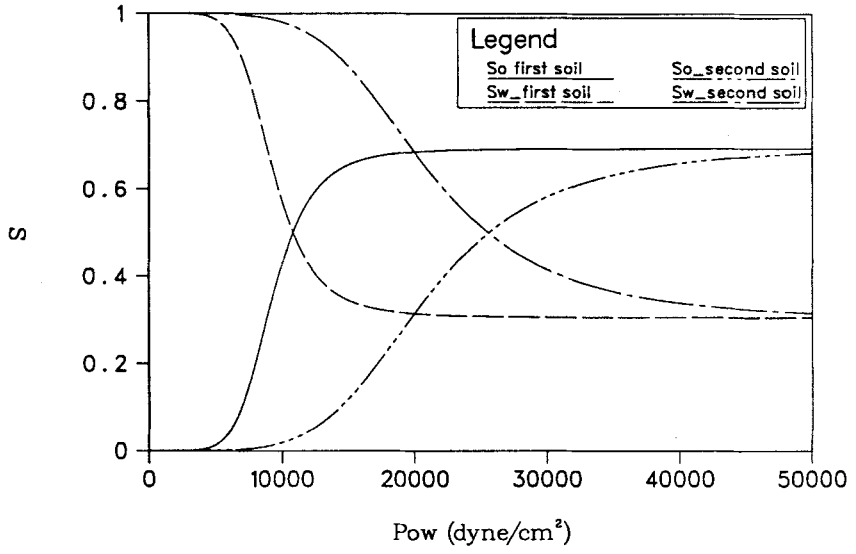

Figure 4. Retention curves for TCE and water in soils 1 and 2

regression form for the curvature weight which depends upon L and n. For the first soil and the fluid characteristics in Table I this expression is given as

$$B = 0{\cdot}2787 \exp\left(-15{\cdot}8576 \frac{\sqrt{L}}{n}\right) \quad (\mathrm{cm}^{-1/2}). \tag{4}$$

The function for the second soil is

$$B = 0{\cdot}00290 \exp\left(-8{\cdot}4540 \frac{\sqrt{L}}{n}\right) (\mathrm{cm}^{-1/2}), \tag{5}$$

where L is given in centimetres. Note that the negative exponential form is the same for both the poorer- and the better-graded soils, but each has different coefficients owing to the differing curvature.

Experimentation showed that for fewer nodes there is a need to increase the weight of the gradient or alternatively to decrease the curvature weights (B_1 and B_2). The reason for this requirement is that a higher proportion of the nodes must be clustered about the front to achieve an accurate solution as the total number of nodes is reduced. On the other hand, there is a need to increase the curvature weights with the number of nodes in order to distribute more nodes in the curvature zones, upstream and downstream of the front. Such a distribution serves to increase the smoothness of the solution in these regions of high curvature. The numerical experiments also showed that the solution is less sensitive to variations in the curvature weights with an increasing number of nodes or with increasing domain length, given a fixed ratio of node number to domain length. Representation of the pressure functions is clearly more accurate with an increased number of nodes. Given the same ratio of node number to domain length, nodal positions may be more easily adjusted to the moving front as the domain length increases. This is because, in a larger domain, much of the length would require only a few nodes to adequately represent the function involved.

For the simulation shown in Figure 1, B_2 was selected as 10^{-4} and B_1 as 20% larger than B_2. In general B_1 should be somewhat larger than B_2 if it is known *a priori* that the front is going to advance in only one direction. This observation results from examination of the solution which is obtained by the fine FGFEM. The fine grid solution shows that more nodes are needed to interpolate the functions in the curvature zone upstream of the front than the number of nodes clustered in this region by nodal redistribution utilizing $B_1 = B_2$. The curvatures of the pressures (and of the saturations) reach their maximum value at the front toe, a phenomenon which tends to cluster more nodes downstream of the front toe. For example, compare the result of the simulation for the case where $B_1 = B_2 = 2{\cdot}5 \times 10^{-5}$ (Figure 5) with the simulation results shown in Figure 1. It is advised that B_1 be set equal to B_2 for cases in which the front movement direction is unknown *a priori* or is expected to change during the simulation.

In addition to the parameter sensitivity highlighted above, the solution quality is also sensitive to the frequency of nodal redistribution. Recall that nodal adaptation is accomplished in a non-simultaneous manner by solution of (2). A number of adaptation schemes could be employed. Re-evaluation of nodal positions could be implemented every iteration within each time step, at the end of each time step or every few time steps, depending upon the results of some specific redistribution test. Nodal position re-evaluation in the example described above was implemented after any time step in which the largest gradient was located in an element whose length was greater than the smallest element length by some percentage, i.e. when the following condition was met:

$$L_i(\max\{P_i'\}) > \min\{L_i\} \times \text{factor}. \tag{6}$$

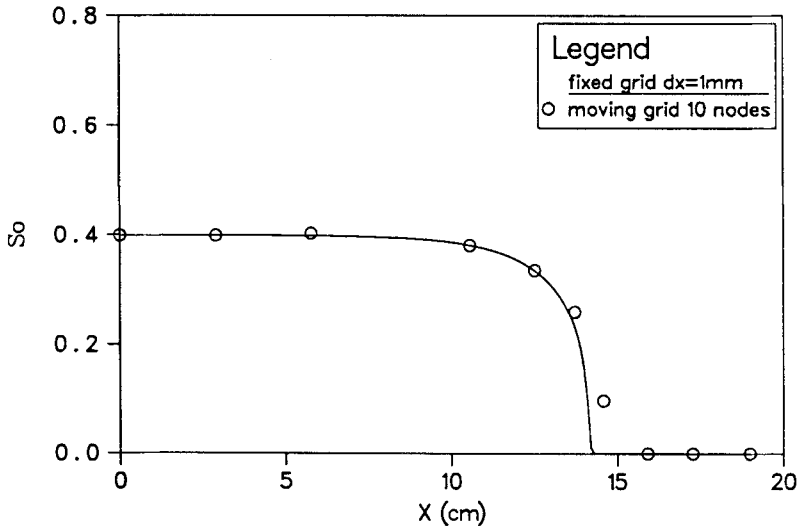

Figure 5. Simulation solution with equal upstream and downstream curvature: simulation solution after $t = 1000$ s for the system shown in Figure 1 with $B_1 = B_2 = 2{\cdot}5 \times 10^{-5}$

Here L_i (max $\{P_i'\}$) is the length of element i which contains the maximum gradient, min $\{L_i\}$ is the smallest element length in the domain and 'factor' is a positive constant greater than 1·0. Simulation results for this nodal redistribution frequency criterion (6) are shown in Figures 1, 2 and 5 for factor = 1·2.

The above redistribution test is suitable for this case since the solution is a single front moving relatively slowly in one direction. A more general test involves evaluation of the maximum deviation from zero of the left-hand side of equations (2). If this deviation is greater than some specified value, nodal locations are then recomputed. This general test facilitates iterative nodal redistribution as necessary (every time step or within a time step). Such a redistribution approach was found to be mandatory for cases involving multiple fronts or changing flow direction.

2. EXAMPLE APPLICATIONS

Vertical scenario—case 2

A vertical single-front scenario was simulated in order to validate the MGFEM for a scenario in which gravity played a role. This case also served to support the utility of the parameter selection guidelines outlined above. Initial and boundary conditions for this simulation are given in Table II. A 45 cm domain length with 15 nodes was selected for the fixed coarse grid and moving grid comparison. The results of this simulation were subsequently employed as initial conditions for a two-front simulation test (case 3).

This simulation employed the more general test for nodal redistribution based upon the deviation of 2(d) from zero. It was incorporated in this simulation in order to examine its performance before employing it for a more complicated scenario. This test was found to consume more computation time than the test based on the smallest element length (6). This is due to the time required for assembly and evaluation of equations (2) after each time step. Grid adaptation was generally performed more frequently than in the previous simulation, where the

grid was adapted only when the front moved downstream to the next element. A value of about 0·3% of the maximum value of the variables was selected as the maximum absolute deviation of 2(d) from zero. This selection was based upon the desire to minimize both the CPU time and the error in the organic chemical saturation solution. An increase in the maximum allowable deviation increased the error in the phases' saturation significantly. Decreasing the deviation factor, however, did not increase the solution accuracy significantly and the computation time increased enormously.

Simulation results for this scenario are shown in Figures 6 and 7 for $t = 1000$ s and the performance comparison is given in Table III. Figure 6 shows the solution of S_o and Figure 7 the

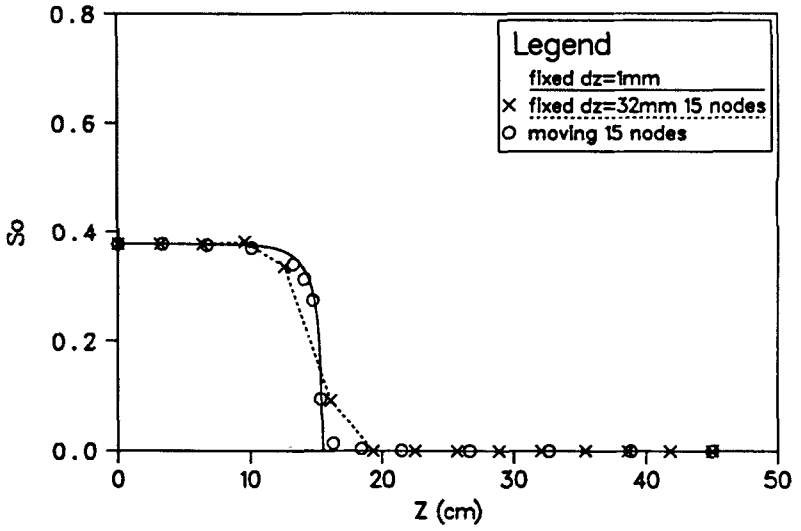

Figure 6. S_o simulation results for case 2 after 1000 s

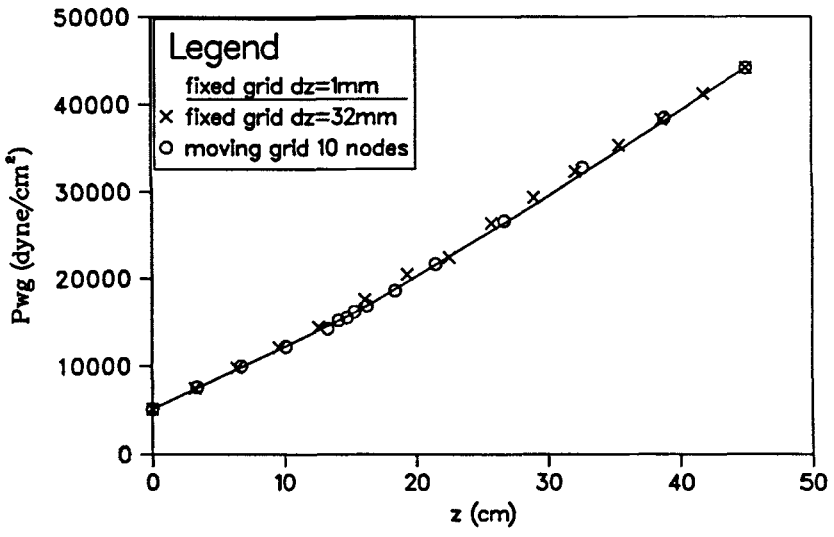

Figure 7. P_{wg} simulation results for case 2 after 1000 s

solution of P_{wg}. The solution of P_{ow} is visually the same as the solution of S_o and can be obtained from $S_w(1-S_o)$ by equation (1c). The selected moving grid curvature parameters were the same as in case 1 because $(\sqrt{L})/n$ has about the same value in both cases. Table III shows that the error in the MGFEM solution for S_o is only 41% of the error in the fixed grid solution. Figure 7 reveals that the differences in the solutions for P_{wg} for the two algorithms are negligible compared to the differences in the solutions for S_o (Figure 6). Similar observations were made in all other two-phase simulations. Thus further results of P_{wg} for two-phase flow problems will not be presented herein. Inspection of the table also reveals that the MGFEM CPU time is 82% more than the fixed grid time, but only 85% of the iterations used for the coarse fixed grid were required. The fixed grid algorithm needed 91 nodes (10816 bytes) and 8216 CPU seconds to obtain a solution of the same accuracy as that obtained by the MGFEM. Thus the MGFEM shows savings of 93·4% in computation time and 80·5% in storage. This numerical simulation example demonstrates the potential of the MGFEM to save a high percentage of computation time even with the more general and time-consuming grid redistribution test.

Two-phase double front—case 3

Subsequent to 1000 s of vertical displacement of water by TCE, another simulation was conducted to model flushing of the TCE with water. This scenario involves the simulation of a two-phase, double-front problem. The fronts are the previously introduced TCE–water front and the new front where the TCE is being replaced by water. Boundary conditions are given in Table II. Note that a residual value of TCE saturation was maintained at the upstream boundary. The new boundary pressure of the water source is just above the previous total boundary pressure and is set at this level in order to prevent backflow of TCE. The moving grid parameters used for this simulation are $\varepsilon_1=\varepsilon_2=0$ and $B_1=B_2=2{\cdot}5\times10^{-5}$, as recommended by the analysis of these parameters given above.

Results after 10 and 1000 s of simulated time are presented in Figure 8 and a performance comparison is given in Table IV. Figure 8 illustrates the good response of the moving grid algorithm to the change in upstream boundary conditions. Figure 8 and Table IV show that the error produced by the moving grid algorithm is much smaller than the error produced by the fixed grid algorithm for the same number of nodes. The smaller error in the MGFEM solution is the result of the motion of nodes toward the boundary after the change in boundary conditions. This redistribution of nodes decreases the amount of organic depletion from the domain after a change in boundary conditions, as illustrated in Figure 9. The fixed grid solution suffered severe undershooting in the solution at early times owing to lack of nodes in this portion of the domain. In this case the error of the moving grid was only 9% of the error associated with the fixed grid after 1000 s of simulation, as indicated in Table IV. The error in the moving grid solution did not

Table III. Comparison between moving and fixed grid FEM simulation case 2

Comparison point	Fine fixed grid	Coarse fixed grid	Moving grid
No. of nodes	451	15	15
Nodal spacing (mm)	1	32	Variable
No. of iterations	10690	3289	2802
CPU time (s)	23753	279	508
Total memory space (bytes)	52576	2000	2110
Error		0·4115	0·1709

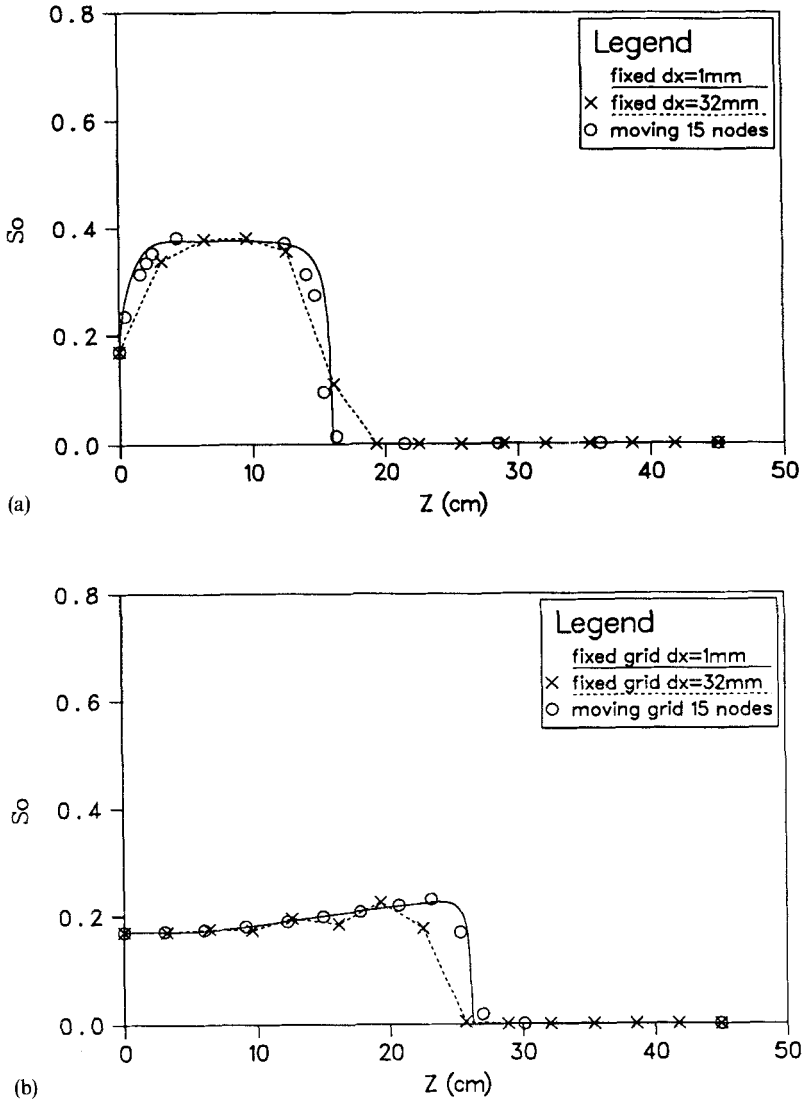

Figure 8. S_o simulation results for case 3 (a) 10 s and (b) 1000 s after creating a second front

Table IV. Comparison between moving and fixed grid FEM simulation case 3

Comparison point	Fine fixed grid	Coarse fixed grid	Moving grid
No. of nodes	451	15	15
Nodal spacing (mm)	1	32	Variable
No. of iterations	8414	3099	2530
CPU time (s)	23218	300	443
Total memory space (bytes)	52576	2000	2110
Error		0·6464	0·0540

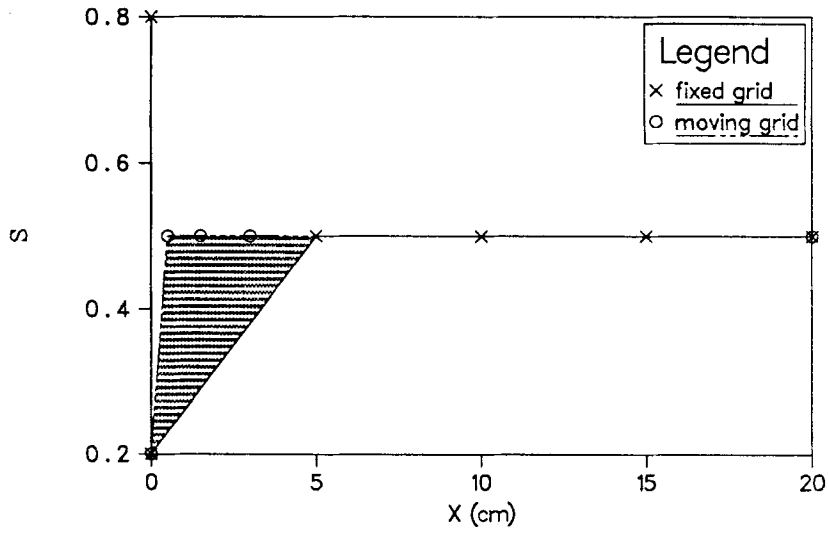

Figure 9. Illustration of organic chemical depletion with grid coarsening

increase much with time during this simulation. This is because the fronts were not as steep as in the single-front problem. Table IV also indicates that with 15 nodes the MGFEM needed only 82% of the iterations used by the coarse FGFEM to simulate the problem. However, the moving grid approach required 48% more computation time owing to the redistribution test calculations. The moving grid simulation of this two-front problem included the momentary fixing of nodes at local maxima and minima as discussed in Part 1 of this paper. This was done to minimize mass balance errors during redistribution.

Two-phase double front with a sink—case 4

Next a simulation test case was conducted to model the operation of a sink within a domain where water displacement by TCE began at an earlier time. This scenario involves the simulation of a two-phase, double-front problem with a sink/source, where the sink is installed to stop the advancement of the front. The initial and boundary conditions for this test were obtained from the solution of case 1 after 1000 s as shown in Figure 1. The moving grid parameters used for this simulation were $\varepsilon_1 = \varepsilon_2 = 0$ and $B_1 = B_2 = 2{\cdot}5 \times 10^{-5}$. The selected sink strength for this case was $0{\cdot}03\ \text{cm s}^{-1}$, which is twice the organic flux at the upstream boundary. This sink was installed at the fifth coarse grid node. The fourth moving grid node was moved artificially to this same location at the start of the simulation. Results for S_o after 50 and 150 s of simulation time are presented in Figure 10. Here, as in the previous example, it was necessary to identify and momentarily fix nodes of local pressure minima and maxima. Such an operation also served to fix the location of the sink node. Examination of Figure 10 reveals that the moving grid solution is less subject to oscillations compared to the fixed grid solution, even with less nodes in the interval between the upstream boundary and the sink. In addition, the moving grid algorithm clusters the nodes about the steeper gradient zone, providing excellent agreement with the fine fixed grid solution. Simulations beyond 150 s showed that the flow reaches an almost steady state condition at this time, with near-residual TCE between the sink and the TCE–water front.

A performance comparison between the MGFEM and the FGFEM is given in Table V. The comparison shows that the error is comparable for both methods after 150 s. The errors are

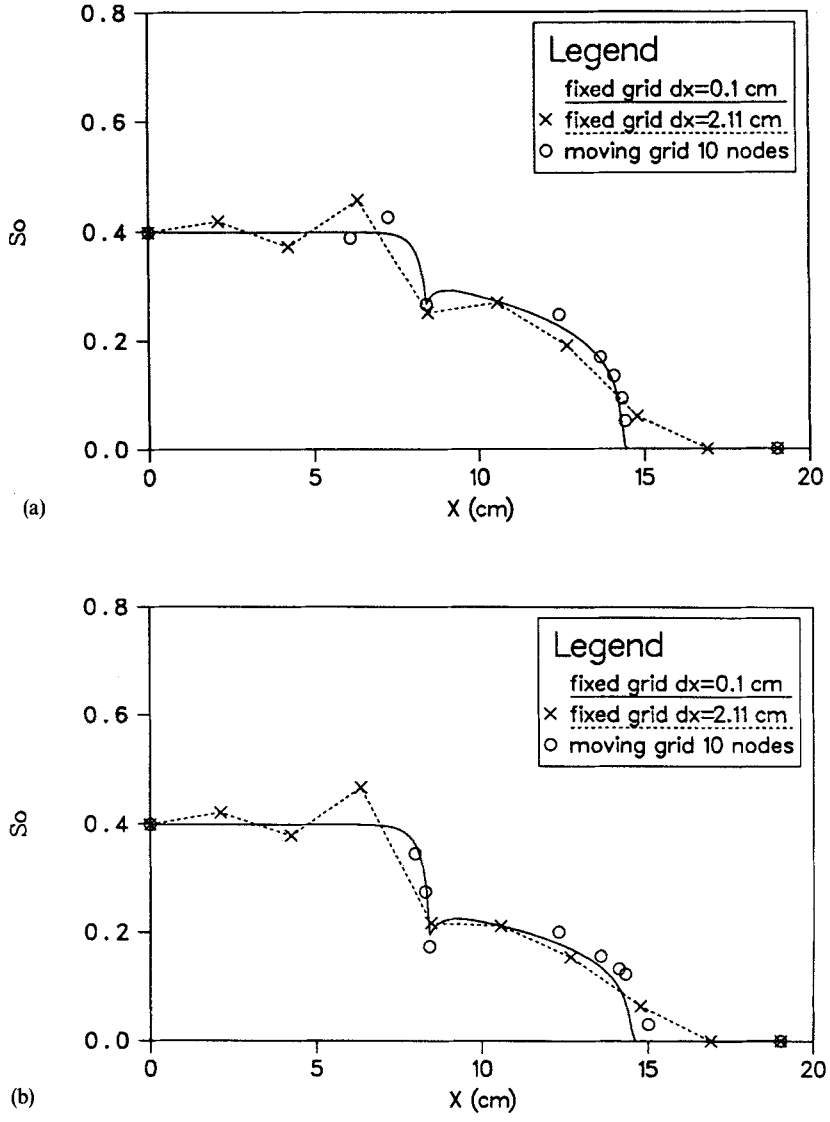

Figure 10. S_o simulation results for case 4 after (a) 50 s and (b) 150 s

Table V. Comparison between moving and fixed grid FEM simulation case 4

Comparison point	Fine fixed grid	Coarse fixed grid	Moving grid
No. of nodes	191	10	10
Nodal spacing (mm)	1	21	Variable
No. of iterations	1789	946	946
CPU time (s)	2845	76	83
Total memory space (bytes)	52576	2000	2110
Error		3·9	4·1

approximately the same even though the MGFEM uses only two-thirds of the nodes employed by the fixed grid solution within the problematic subdomain between the upstream boundary and the sink. With equal numbers of nodes in this interval the MGFEM gives a superior solution, as is illustrated in Figure 11 where a moving grid node was artificially moved upstream of the sink prior to the simulation. In this simulation the error of the MGFEM is only 2% of the error associated with the coarse FGFEM solution upstream to the sink point and 20% of the FGFEM error for the entire domain.

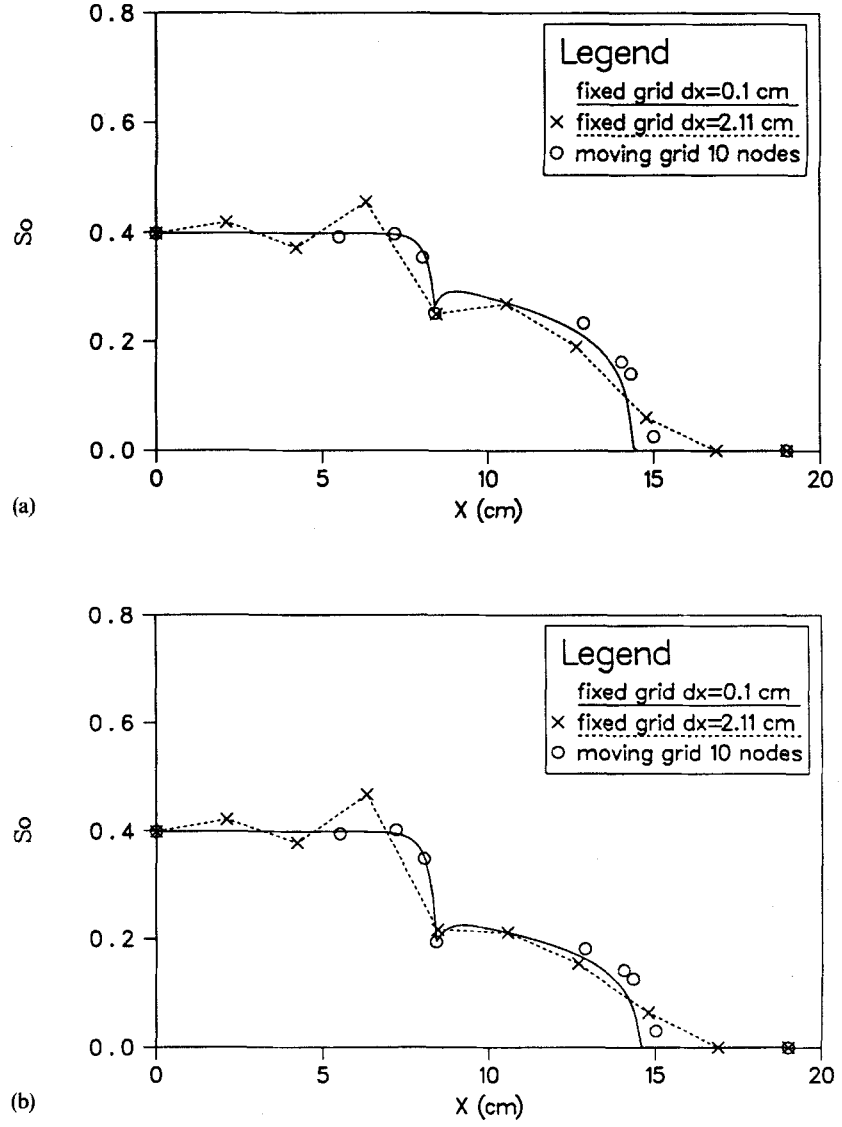

Figure 11. S_o simulation results for case 4 with an equal number of moving and fixed nodes upstream of the sink after (a) 50 s and (b) 150 s

Three-phase single front—case 5

This three-phase flow test case involves simulation of horizontal, single-front, TCE displacement of gas in an unsaturated soil column. TCE invades from an upstream boundary source with a fixed head into a 48 cm soil column where all fluid phases are present initially. Initial and boundary conditions are given in Table II. The downstream boundary and initial conditions correspond to 30% water, 10% TCE and 60% gas saturations, while the upstream boundary conditions correspond to 30% water, 58% TCE and 12% gas saturations. The selected moving grid parameters are $\varepsilon_1=(1/100\max\{P'\})^2$ as specified in equation (3), $\varepsilon_2=0$ and $B_1=B_2=5\times10^{-6}$ as specified in equation (4). Simulation results for this case are shown in Figure 12 for 100, 500 and 1000 s and a performance comparison is given in Table VI. Note that Figure 12 shows the results for S_w, S_o and S_g. The solution of P_{ow} can be recovered from equation (1c) using $S_\alpha=S_w$, and the solution of $P_{ow}+P_{wg}$ can also be recovered from equation (1c) using $S_\alpha=S_w+S_o$.

An iterative algorithm and repulsive force were incorporated in the moving grid scheme to solve the three-phase flow problem. Iterations on grid redistribution were made within a time step to correct the representative gradient estimates relative to the new element lengths. These gradients changed significantly during each grid adaptation iteration about the front, especially at the beginning of the simulation, and iterations were needed in order to assure equidistribution of the gradient and curvature for the new nodal positions. Without these iterations, equidistribution according to equations (2) was not achievable in a single grid adaptation operation. During the first grid adaptation, most of the nodes moved to a very small interval near the upstream boundary owing to the imposition of the boundary condition. Without interactive adaptation the nodes then moved back to an almost equal spacing distribution within the next few grid adaptations and returned to a very small interval by the upstream boundary in an oscillatory manner. Such grid oscillations will create severe numerical errors as the simulation proceeds.

The repulsive force was required in these simulations to avoid a singular or ill-conditioned nodal redistribution matrix (equations (2)) due to the presence of zero gradient and curvature values. In the development of the governing equations (1) it was assumed that the gas phase would remain at a constant (atmospheric) pressure. Thus, when TCE displaces this fluid, no gradient is created in the gas phase pressure and all gradients downstream of the organic front remain zero. Figure 12 also shows that the front of organic advancement smears faster than in the organic–water front case (Figure 1) and thus equidistribution with respect to curvature is less important.

The numerical results show good agreement between the MGFEM and the fine fixed grid solutions. This can be seen in Figure 12 and Table VI. Table VI shows that the error in the MGFEM solution is only 4·3% of the fixed grid FEM solution when both employ nine nodes. For this problem the MGFEM scheme used more iterations and more CPU time. However, the FGFEM requires 51 nodes, 6788 bytes and 1084 CPU seconds to obtain a result with the same accuracy as the MGFEM result with nine nodes. This translates to a fixed grid requirement of 274% more memory bytes and 323% more CPU time than used by the moving grid. These figures demonstrate significant savings of computer resources by the MGFEM simulator for a one-dimensional three-phase flow with a single front.

Three-phase double front—case 6

A final simulation test case examined the flushing of TCE with water after a previous gas displacement by TCE. The simulation was conducted for a horizontal case where the initial conditions were the results of the three-phase, single-front simulation (case 5). This scenario

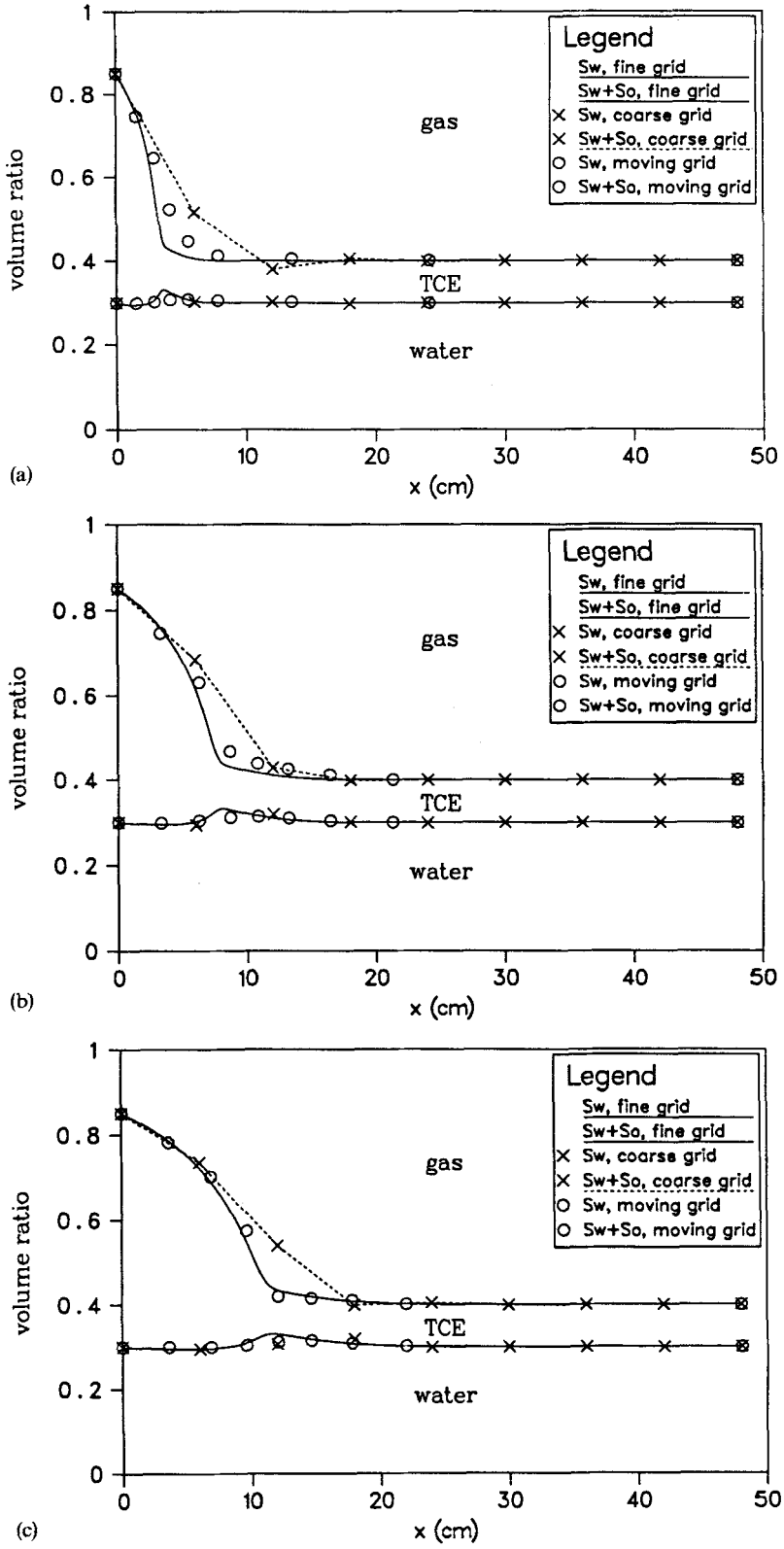

Figure 12. Simulation results for case 5 after (a) 100 s, (b) 500 s and (c) 1000 s

Table VI. Comparison between moving and fixed grid FEM simulation case 5

Comparison point	Fine fixed grid	Coarse fixed grid	Moving grid
No. of nodes	481	9	9
Nodal spacing (mm)	1	32	Variable
No. of iterations	2388	2082	3082
CPU time (s)	15057	169	258
Total memory space (bytes)	61828	1412	1816
Error		1·3092	0·0563

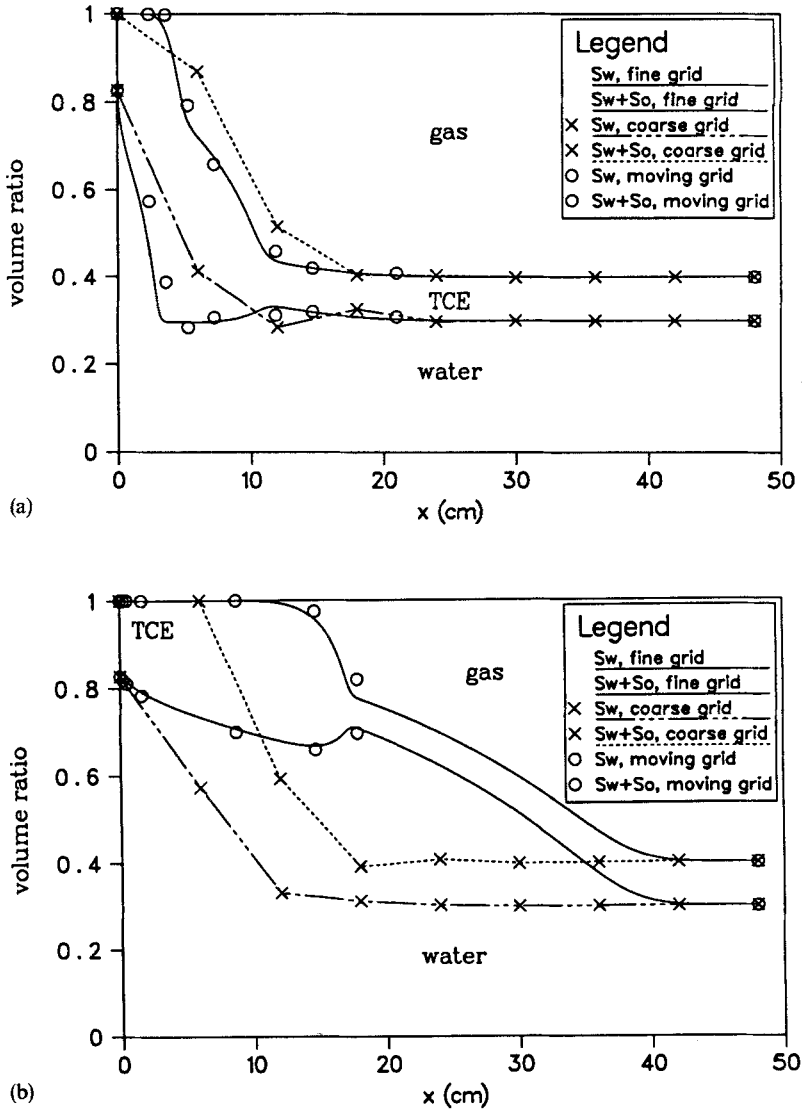

Figure 13. Simulation results for case 6 (a) 10 s and (b) 1000 s after creating a second front

Table VII. Comparison between moving and fixed grid FEM simulation case 6

Comparison point	Fine fixed grid	Coarse fixed grid	Moving grid
No. of nodes	481	9	9
Nodal spacing (mm)	1	32	Variable
No. of iterations	8642	2756	2629
CPU time (s)	51834	292	250
Total memory space (bytes)	61828	1412	1816
Error		0·9268	0·2561
Error		0·9268	0·2561

involves the simulation of a three-phase, double-front problem. The fronts are the previously introduced gas–TCE–water front and the new front where the TCE is being replaced by water. Boundary conditions are summarized in Table II. The upstream boundary is fully saturated with water and the new boundary pressure of the water is set just above the previous total boundary pressure so as to prevent backflow of TCE or gas. The moving grid parameters used for this simulation are the same as in the previous single-front, three-phase problem.

Results after simulation times of 10 and 1000 s are shown in Figure 13 and a performance comparison is given in Table VII. Figure 13 shows the good response of the moving grid algorithm to the change in the upstream boundary conditions. The figure and the table demonstrate that the error produced by the moving grid algorithm is again much smaller than the error produced by the fixed grid algorithm for the same number of nodes. The behaviour here was very similar to the two-front, two-phase scenario (case 3) described previously. Severe mass balance errors resulted in the coarse fixed grid solution owing to the lack of nodes near the upstream boundary. After 1000 s of simulation the error of the moving grid solution was only 27% in S_o and 11% in S_w of the associated error with the fixed grid. The error in the moving grid solution did not increase much during this simulation, similar to experience with the two-phase, double-front simulation.

3. CONCLUSIONS

In Part 2 of this paper, example simulations have been presented to compare the performance of the MGFEM with a standard fixed grid scheme. Test cases examined include single- and multiple-front problems involving two- and three-phase flow regimes. The examples demonstrate the capability of the MGFEM to simulate a variety of one-dimensional multiphase flow scenarios in porous media and its potential to save computer resources. More accurate results were consistently obtained with the MFGEM than with the FGFEM in all simulations examined for the same number of degrees of freedom. In addition, the MGFEM achieved significant savings in computer resources when compared with alternative FGFEM solutions of the same accuracy.

The simulations justify the selection of the maximum gradient, from among all the primary variable gradients, as the representative gradient for the moving grid adaptation, as was suggested in Part 1 of this paper. Momentary fixing of nodes associated with extremum pressures was shown to overcome mass balance problems in multiple-front simulations. This approach also served to fix a sink node during the redistribution process.

A sensitivity analysis was conducted to develop guidelines for the selection of MGFEM parameters for simulations involving multiphase flow in porous media. On the basis of this analysis the following conclusions were drawn.

1. The artificial repulsive force ε_1 should be zero for simulating multiphase flow in the absence of a gas phase. When a gas phase is present, this parameter should be related to the ratio between the gas and water viscosities multiplied by the maximum water gradient in the domain (see equation (3)). This choice of ε_1 compensates for the neglect of the gaseous pressure gradient in the governing equations. It assures that the set of nodal redistribution equations (2) will not become ill-conditioned as the result of a zero gradient.
2. The artificial viscosity ε_2 should be set to zero for all simulations.
3. The curvature weights B_1 and B_2 should be reduced when the number of nodes in the domain increases. Optimal weights were shown to exhibit an exponential dependence on $(\sqrt{L})/n$ (see equations (4) and (5)). Soil grading was also shown to be a factor in the selection of these parameters.

Future investigations will be required to increase the flexibility of the MGFEM approach. Further work will be needed to develop a functional form for the curvature weights, which would depend upon gradient and curvature magnitudes and distributions in the simulation domain. This development is necessary to eliminate the need for *a priori* determination of these weights and would facilitate the self-adaptive evolution of the algorithm to changes in the magnitude and distribution of curvature and gradient. Another possible extension of the work contained herein would be to explore the application of the MGFEM approach to other types of coupled non-linear PDE problems. It is anticipated that moving grid parameter selection guidelines would have to be developed on an application-specific basis.

Extension of the moving grid model to two spatial dimensions would require expansion of the equidistribution equation to higher dimensions. This would involve determination of suitable first- and second-degree error estimators in multidimensions, formulation of element error equidistribution criteria (see e.g. equations (17) and (19) in Part 1), development of discrete analogues to the equidistribution criteria (see e.g. equation (21) in Part 1) and integration of these criteria and combination into one criterion (see e.g. equation (24) in Part 1). This will result in a set of algebraic equations to distribute the nodes according to any of the variables in the problem. Determination of a representative variable to form a single set of equations would then be required. Two-dimensional 'expanding grid' adaptation models have previously been developed for a limited number of problems governed by a single PDE (e.g. References 9–11). Such models, however, did not have to overcome grid adaptation with respect to different variables or mass conservation errors with grid adaptation, which are major problems in the solution of the non-linear coupled set of PDEs governing multiphase flow in porous media. In addition, these models were utilized to solve problems involving straight line boundaries where two-dimensional elements may stretch almost uniformly across the domain in the solution of a single-front problem. Our model could easily be extended to this kind of two-dimensional problem. Unfortunately, grid deformation may be considerable in general two-dimensional multiphase flow problems and boundary nodes must be fixed to describe the location of irregular boundaries and spatial variations in the boundary conditions. Thus model extension to generalized problems in two dimensions would most likely require incorporation of a routine to recalculate local element nodal connectivities.

ACKNOWLEDGEMENTS

This work was supported in part by grant ECE-8451469 from the National Science Foundation with matching funds from the Electric Power Research Institute under contract RP2377-5. The paper has not been subject to EPRI review and thus the views and opinions expressed herein do not necessarily reflect those of EPRI.

APPENDIX: DIMENSIONAL ANALYSIS OF EQUATION (1) OF PART 1

Neglecting the compressibility and gravity terms, equation (1) of Part 1 can be written as

$$\phi \frac{\partial S_\alpha}{\partial t} = \frac{K}{\mu_\alpha}\left(k_{r_\alpha}\frac{\partial P_\alpha}{\partial x}\right). \tag{7}$$

Now the following scaling and dimensionless variables may be defined: L, domain length; $l = L/n - 1$; λ, front velocity; $p_\alpha = p^*\mu_\alpha\lambda/l$; $t = t^*\Delta\rho l^2/\mu_w$; $x = x^* l$; $K = K^* l^2$. Here $\Delta\rho$ is the density difference between the wetting and non-wetting fluids. Substituting the dimensionless variables in (7) yields

$$\frac{\phi\mu_w}{\Delta\rho}\frac{\partial S_\alpha}{\partial t^*} = \frac{l^2 K^*}{\mu_w\mu_\alpha/\mu_w}\frac{\mu_w\lambda}{l}\frac{1}{l^2}\frac{\partial}{\partial x^*}\left(k_{r_\alpha}\frac{\partial P^*}{\partial x^*}\right). \tag{8}$$

Reorganization of (8) yields

$$\frac{\partial S_\alpha}{\partial t^*} = \frac{\mu_w/\mu_\alpha}{\phi}\frac{\lambda\Delta\rho l}{\mu_w}K^*\frac{\partial}{\partial x}\left(k_{r_\alpha}\frac{\partial P^*}{\partial x^*}\right)$$

or

$$\frac{\partial S_\alpha}{\partial t^*} = \frac{\mu_w/\mu_\alpha}{\phi}\mathscr{R}e K^*\frac{\partial}{\partial x^*}\left(k_{r_\alpha}\frac{\partial P^*}{\partial x^*}\right), \tag{9}$$

where $\mathscr{R}e = \lambda\Delta\rho l/\mu_w$ can be considered as a Reynolds number.

Here similarity requires that the Reynolds number of the scaled variables multiplied by the viscosity ratio divided by the porosity be the same. Note that the front velocity depends upon the initial and boundary conditions, the intrinsic permeability and the relative permeability and saturation functions of the capillary pressure.

REFERENCES

1. S. Adjerid and J. E. Flaherty, 'A moving mesh finite element method with local refinement for parabolic partial differential equations', *Comput. Methods Appl. Mech. Eng.*, **55**, 3–26 (1986).
2. A. C. David and J. E. Flaherty, 'A two dimensional mesh moving technique for time dependent partial differential equations', *J. Comput. Phys.*, **67**, 124–144 (1986).
3. L. R. Petzold, 'Observation on an adaptive moving grid method for one-dimensional systems of partial differential equations', *Appl. Numer. Math.*, **3**, 347–360 (1987).
4. J. G. Bloom, J. M. Sanz-Serna and J. G. Verwer, 'On simple moving grid methods for one-dimensional evolutionary partial differential equations', *J. Comput. Phys.*, **74**, 191–213 (1988).
5. R. Miller, 'Moving finite elements. II', *SIAM J. Numer. Anal.*, **18**, 1033–1057 (1981).
6. G. F. Carey, A. Mueller, K. Sepehrnoori and R. L. Thrasher, 'Moving elements for transport processes', *SPE Reservoir Eng.*, **2**, 401–403 (1987).
7. J. Kautsky and N. K. Nichols, 'Equidistribution meshes with constraints', *SIAM J. Sci. Stat. Comput.*, **1**, 499–511 (1980).
8. A. Gamliel, 'Simulation of immiscible multiphase flow in porous media using a moving grid finite element method', *Ph.D. Thesis*, Department of Civil Engineering, The University of Michigan, 1989.
9. J.-H. Cheng, 'Automatic adaptive remeshing for finite element simulation of forming processes', *Int. j. numer. methods eng.*, **26**, 1–18 (1988).
10. M. J. Djomehri and J. H. George, 'Application of the moving finite element method to moving boundary Stefan problem', *Comput. Methods Appl. Mech. Eng.*, **71**, 125–136 (1988).
11. D. C. Arney and J. E. Flaherty, 'Mesh moving technique for time dependent partial differential equations', *J. Comput. Phys.*, **67**, 124–144 (1988).
12. L. M. Abriola, *Multiphase Migration of Organic Compounds in Porous Medium, a Mathematical Model*, Lecture Notes in Engineering, Volume 8, Springer, Berlin, 1984.